Copyright © 2000, by the author(s).
All rights reserved.

Permission to make digital or hard copies of all or part of this work for personal or classroom use is granted without fee provided that copies are not made or distributed for profit or commercial advantage and that copies bear this notice and the full citation on the first page. To copy otherwise, to republish, to post on servers or to redistribute to lists, requires prior specific permission.

STROBOSCOPIC INTERFEROMETER SYSTEM FOR DYNAMIC MEMS CHARACTERIZATION

by

Matthew R. Hart, Robert A. Conant, Kam Y. Lau
And Richard S. Muller

Memorandum No. UCB/ERL M00/18

20 April 2000

STROBOSCOPIC INTERFEROMETER SYSTEM FOR DYNAMIC MEMS CHARACTERIZATION

by

Matthew R. Hart, Robert A. Conant, Kam Y. Lau, and Richard S. Muller

Memorandum No. UCB/ERL M00/18

20 April 2000

ELECTRONICS RESEARCH LABORATORY

College of Engineering
University of California, Berkeley
94720

Stroboscopic interferometer system for dynamic MEMS characterization

Matthew R. Hart, Robert A. Conant, Kam Y. Lau, Richard S. Muller

Abstract-- We describe a computer-controlled stroboscopic phase-shifting interferometer system for measuring out-of-plane motions and deformations of MEMS structures with nanometer accuracy. To aid rapid device characterization our system incorporates: (1) an imaging interferometer that records motion at many points simultaneously without point-by-point scanning, (2) an integrated computer-control and data-acquisition unit to automate measurement, and (3) an analysis package that generates sequences of time-resolved surface-height maps from the captured data. The system can generate a detailed picture of microstructure dynamics in minutes. A pulsed laser diode serves as the stroboscopic light source permitting measurement of large-amplitude motion (tens of μm out-of-plane) at kHz frequencies. The high out-of-plane sensitivity of the method makes it particularly suitable for characterizing actuated micro-optical elements for which even nanometer-scale deformations can produce substantial performance degradation. We illustrate the capabilities of the system with a study of the dynamic behavior of a polysilicon surface-micromachined scanning mirror that was fabricated in the MCNC MUMPS foundry process.

Index Terms—MEMS motion characterization, stroboscopic interferometer system

I. Introduction

The need to improve the reliability and predictability of MEMS devices has prompted research into suitable motion-characterization tools. To help us understand the mechanical properties of typical MEM systems, these tools must be able to measure submicron displacements of features that range in size from a few microns to a few millimeters. To allow us to observe system dynamics, they must be capable of time-resolved measurement. In addition, if we are to study motions that are more complex than simple rigid-body translations, our characterization tools need to permit independent measurements of displacement or velocity at multiple points on a structure.

Time-resolved measurement techniques can be subdivided into two categories: (1) real-time methods that allow measurements of arbitrary motions, and (2) time-averaged techniques that rely on an assumed property of the motion, for example, a known periodicity. An example of a technique in the former category is laser Doppler vibrometry (LDV), which has been used extensively for the characterization of both macro- and micromechanical systems [1, 2]. The LDV technique makes use of the Doppler frequency shift that occurs when a light beam is reflected from an object moving along the beam axis. When such a

beam is recombined on a square-law detector with light from the same source that has not been frequency shifted (or, alternatively, light that has been shifted a different amount using an acousto-optic modulator), a time-varying interference signal is generated. This signal varies sinusoidally at a frequency equal to the frequency difference between the recombined beams. This beat frequency can be used to determine the component of velocity along the direction of the incident beam. Because the beat frequencies generated by the LDV technique are large (typically in the tens of MHz range), a fast detector is needed to capture the time-varying interference signal. The lack of sufficiently fast array detectors (cameras) limits the method to measuring the motion of a single point (or a small number of points) at a time, the frame rates of presently available high-speed cameras being much too slow for a full-field (imaging) implementation of LDV. Scanning vibrometers that use a raster-scanning technique to sweep the measurement beam over a two-dimensional area, one point at a time, are available. However, use of a sequential raster scan eliminates one major advantage of the LDV method, that of real-time measurement.

If the motion to be measured is repeatable, any one of a number of time-averaging techniques can be used. For example, stroboscopic methods are useful when structures move periodically. Since, in the stroboscopic method, the minimum resolvable time interval can be governed by the light-pulse width rather than by the detector integration time, the detector need not be fast compared to the motion being analyzed. A conventional CCD camera with a frame rate of 30 Hz can be used to measure motions in the range of hundreds of kHz, when it is combined with a solid-state light source such as a laser- or light-emitting diode (LED).

Freeman et al. [3, 4] have demonstrated a MEMS-characterization system based on a conventional light microscope modified by the addition of an LED light source. In this system, the microdevice is driven with a periodic force and the LED is pulsed at the same frequency so that the device is illuminated only at one specific phase of motion. By adjusting the relative timing of the LED pulse train and the drive force, this phase can be varied, allowing a sequence of images depicting the motion over the interval studied to be captured. Image-processing algorithms are then used to find least-squares-fit translation and rotation parameters between adjacent pairs of stroboscopic images [5]. In-plane rigid-body motion of the microdevice can be recovered from a set of these least-squares-fit parameters. Davis and Freeman have reported the ability to track in-plane translation with random errors as small as 2 nm [3]. By taking stroboscopic images at a number of different focal planes, Freeman et al. [4] have also shown that the technique can be used to track rigid-body motion that includes an out-of-plane component. The lowest reported noise floors for out-of-plane motion, using this method, are on the order of 5 nm [6].

Although this technique can provide valuable information about MEMS motion, it does have a number of drawbacks. First, the image processing required is computationally intensive, normally limiting the method to analysis of small regions on the test device. Second, systematic measurement error (which can be much larger than the random error [5]) is a function of the spatial frequency content of the captured images (related to the shape of the moving part being measured). Third, the best resolution demonstrated for out-of-plane motion (on the order of 5 nm) is significantly lower than that attainable with optical interferometry [6]. Finally, the technique recovers only the least-squares-fit rigid-body component of the motion and does not account for deformations of the measured structure.

Often, accurate understanding of the behavior of MEMS devices requires knowledge not only of rigid-body motions, but also of dynamic deformations of the moving structures. The method we use, imaging stroboscopic interferometry [7], is attractive for measuring out-of-plane motion and deformation, because of its high sensitivity and its ability to acquire data at many measurement points simultaneously. In an imaging interferometer, the test sample reflects a light beam that is combined with a second beam having a known wavefront, for example, one generated by reflection from a precisely planar reference mirror. Unlike the LDV technique, in this method the whole area of the test structure is illuminated at one time, and imaged onto a 2-D detector array. Due to the interference between the test- and reference-beams, this image is crossed by a series of bright and dark fringes that encode the relative surface-height variations of the test and reference surfaces. Many different techniques can be used to decode this fringe information and to recover a map of the test-surface height [8]. The extreme out-of-plane sensitivity of optical interferometry allows displacement measurements to be made with resolution on the order of 1 nm.

Both Gutierrez et al. [9] and Hemmert et al. [6] have reported LED-based stroboscopic interferometers for measuring small-amplitude resonances (2 μm or less) of micromachined structures. In a previous paper we demonstrated a laser-diode-based stroboscopic interferometer system that could be used to measure large-amplitude (greater than 10 μm) motion of fold-up, surface-micromachined structures [10], with nanometer accuracy. We also showed that the system could measure dynamic out-of-plane deformation. In this paper, we present a detailed description of this interferometer system and discuss how it may be used for both static and dynamic MEMS characterization. By using a laser diode as the stroboscopic source, our interferometer gains a number of advantages over previously reported LED-based systems. First, the higher output powers of laser diodes permit us to use lower duty-cycle pulse-trains than would be possible using LED illumination for the same average beam power. This improves measurement accuracy by giving a better approximation to true impulsive position sampling. Second, the greater modulation bandwidths of laser diodes allow for shorter light pulses, permitting larger out-of-plane velocities to be measured. Third, the higher coherence lengths of these sources facilitate characterization of large amplitude motions.

In Section II, we describe our optical setup and the computer-control unit that permits rapid device characterization. Section III outlines the methods we use for data analysis. We show how phase-measuring algorithms combined with spatial and temporal phase-unwrapping techniques can be used to produce a detailed picture of device motion and deformation from a set of captured interferograms. Finally, in Section IV we demonstrate the capabilities of the system with an analysis of the static and dynamic properties of a fold-up surface-micromachined scanning mirror.

II. COMPUTER-CONTROLLED INTERFEROMETER

A. *Optical configuration*

A schematic of our MEMS-characterization setup is shown in Figure 1. At the heart of the system is a Twyman-Green interferometer formed by a polarizing beamsplitter cube, two quarter-wave plates, a flat reference mirror and the MEMS device under test. The interferometer is illuminated by a 658 nm laser diode (Hitachi HL6501MG) which can be driven in pulsed or continuous-wave (CW) modes. Light from the laser is coupled into a single-mode optical fiber that acts as a spatial filter, eliminating the ellipticity and astigmatism present in the light emitted by the laser diode and producing a near-gaussian beam at its output. An infinity-corrected microscope objective (MO) collects and collimates the fiber output, producing a parallel, circular beam that illuminates the test and reference surfaces. To obtain high-contrast interference fringes, the amplitudes of the beams returned from the test and reference arms need to be well-matched. In our system, matching is achieved using the rotatable half-wave plate (HWP) to alter the polarization angle of the light before it enters the polarizing beamsplitter (PBS). Thus, the split ratio can be varied over a continuous range. We can make measurements of samples with reflectances ranging from about 5 to 100%. The quarter-wave plates (QWP) in each arm of the interferometer are aligned with their optic axes at 45 degrees to the polarization axes of the beamsplitter. This arrangement ensures that light reflected from the test and reference surfaces does not return along the input path, but instead is delivered to the CCD camera (Cohu 6612-1000 with sensor faceplate removed).

The one-inch diameter reference mirror is flat to an accuracy better than 30 nm. It is mounted on two translation stages, one mechanical and one piezoelectric; both of these stages allow the mirror to be translated along the optical axis. The mechanical stage is used to balance the optical-path lengths in the interferometer arms to within a small fraction of the laser-diode coherence length (a few hundred microns) so that high-contrast interference fringes can be generated. The piezoelectric stage (Polytec PI P-

753.11C), which operates under closed-loop control with feedback from a capacitative sensor, is used during measurement to produce a sequence of precise $\pi/2$ phase shifts in the interference pattern as discussed in section III.

The two-lens system, shown in Figure 1 to the right of the beamsplitter, forms a magnified image of the test surface on the CCD array. Since the beams from the two arms leave the interferometer in orthogonal polarization states, a linear polarizer (POL) is placed directly in front of the camera and angled at 45 degrees to the polarization axes so that the interference pattern can be observed. Our setup permits us to image test structures onto the CCD array at nominal magnifications of 5× and 3×. At the 5× magnification setting, we have a field-of-view of approximately 1.3×1.0 mm, with a smallest resolvable feature size of 2 μm. At this magnification, the limiting factor on the image-plane resolution of the system is the CCD pixel size (9.9 μm) rather than the numerical aperture of the optics. The whole system is mounted on a vibration-isolation table and placed in an enclosure to minimize the influences of external vibrations and air currents.

B. Computer control and data capture system

For rapid data acquisition, both the interferometer and the test device are controlled by a single PC. This PC contains a frame grabber (Matrox Meteor II/MC) that digitizes the signal from the CCD camera, an IEEE 488 interface to control the piezoelectric stage, and a digital waveform generator (National Instruments PCI-MIO-16E-1) that supplies the control signals for both the MEMS device and the laser diode during dynamic testing. MEMS driven by signals smaller than ±10V and currents smaller than 5 mA are connected directly to the waveform generator. For MEMS devices designed to operate at higher voltages, our system incorporates a high-voltage amplifier, extending the range of available signals to ±150V.

A graphical user interface (GUI) running on the PC gives the user control over the form, amplitude, and frequency of the MEMS drive signal. Our present implementation provides three drive options: sine and square waves, and near-dc ramped signals. The ramp mode is used to take quasistatic measurements in order to check a MEMS device for linearity and hysteresis. In the sine- and square-wave drive modes, the waveform generator also outputs a trigger signal that governs the relative timing of the MEMS drive signal and the laser-diode pulse train. This timing can be varied using software, either automatically or via the GUI, so that the test device can be observed at many different phases of its motion cycle. Using the sine-wave drive option, our system can drive devices at frequencies between 120 Hz and 30 kHz, for direct measurement of individual resonant modes.

The control software can automatically acquire up to 64 time-resolved measurements over a range of time delays that span one complete period of the motion.

The square-wave option can be used to measure the broad-spectrum frequency response of a device through observation of mechanical ringing after the falling edge of the drive signal. The frequency response, for any point on the test surface, is calculated from a Fourier transform of the measured *(position, time)* vector, the highest observable frequency being governed by the effective rate at which the motion is sampled. This effective sampling rate is determined by the minimum available time-delay increment between the MEMS drive signal and the laser pulse train. The delay increment, in turn, is governed by the update rate of the digital waveform generator (the rate at which the output voltage is changed) which can be varied up to 10^6 updates per second. This allows us to sample motion at frequencies as high as 500 kHz. In the square-wave drive mode, the control software provides for a sequence of up to 512 measurements of the test device to be taken automatically as the time delay between the MEMS drive signal and the laser trigger pulse is varied. For a sequence of N measurements, the cutoff frequency f_{max} can be traded off against frequency resolution $\Delta f=2f_{max}/N$ by varying the waveform generator update rate. Higher update rates give larger values of f_{max} at the expense of larger Δf and higher excitation repetition frequencies. This repetition frequency should be chosen low enough that the device can adequately settle before being driven again by the next voltage step in the square wave.

III. DATA ANALYSIS

A. Principle of measurement using phase-shifting interferometry

To illustrate how the interferometer is used for MEMS characterization, we consider first the problem of determining the surface shape of a static MEMS device. To make the measurement, the device is first placed in the test arm of the interferometer and aligned using a two-axis tilt stage so that the beam reflected from it is coaxial with the reference beam. Then, its along-axis position is adjusted to bring its image into focus on the CCD array. That image is crossed by a series of bright and dark interference fringes caused by the surface-height variations of the device, relative to the flat reference mirror. If we denote the co-ordinates in the plane of the CCD array as (x,y), we can write the intensity of the interference pattern $I(x,y)$

$$I(x,y) = A(x,y) + B(x,y)\cos[\psi(x,y) + \phi] \qquad (1)$$

In equation (1), $A(x,y)$ and $B(x,y)$ are governed by the spatial variations in amplitude of the beams returned from the two interferometer arms and $\psi(x,y)$ is a spatially modulated phase term that encodes the surface-height variations over the test device. The phase term ϕ, constant across the image, is a linear function of the path imbalance between the interferometer arms and can be controlled by axial displacement of the reference mirror using the piezoelectric stage. Each image that is captured and digitized by the frame grabber is an intensity map, described by equation (1).

To extract the surface-height information contained in $\psi(x,y)$ from measurements of the intensity distribution $I(x,y)$, we use a technique known as phase-shifting interferometry [11]. Consider taking a sequence of measurements $I_m(x,y)$ such that the phase at each point in the interference pattern is stepped through an interval of $\pi/2$ radians between successive values of m. Expressed as a function of the initial phase $\theta_1=\psi(x,y)+\phi$ this procedure generates an alternating sequence of sine and cosine terms on the right-hand-side of equation (1). Three such measurements, at phases θ_1, $\theta_2=(\theta_1+\pi/2)$, and $\theta_3=(\theta_1+\pi)$ are sufficient to generate a set of simultaneous equations that can be solved for the initial phase term $(\psi(x,y)+\phi)$. This phase term can, in turn, be used to map the surface-height variations of the test part.

In practice, it is usual to take measurements at more than three values of θ_m so that the problem is overdetermined, making the phase calculation more robust. In the experiments reported here, we used sets of five measurements and calculated the phase using the five-sample algorithm due to Hariharan [12]. As mentioned above, the required phase shifts were generated by stepping the reference mirror to five distinct positions, using a piezoelectric stage. From a sequence of images $I_1(x,y)\ldots I_m(x,y)\ldots I_5(x,y)$, with $\theta_m=\theta_1+(m-1)\pi/2$, we calculate the phase map using Hariharan's algorithm [12]

$$[\psi(x,y)+\phi]= \tan^{-1}\left(\frac{2(I_2-I_4)}{2I_3-I_5-I_1}\right)+2n(x,y)\pi \qquad (2)$$

where the explicit spatial dependence of the intensity terms has been omitted for compactness. The last term of equation (2) includes a spatially varying integer $n(x,y)$ that cannot be measured by the system, but must instead be inferred from *a priori* knowledge of the test surface. This term (which can be recovered using spatial phase-unwrapping techniques) is present because the optical phase can only be measured modulo 2π in a single-wavelength interferometer. Using phase-measuring algorithms

such as that given in equation (2), it is possible to determine interference phases with extremely high precision, and measurement repeatabilities better than one hundredth of a wavelength are commonly reported in the literature [11].

B. *Spatial phase unwrapping*

As we have pointed out, the sequence of interferograms $I_1(x,y)...I_m(x,y)...I_5(x,y)$ captured by the frame grabber is sufficient to calculate only the first term on the right-hand-side of equation (2) (known as the wrapped phase). To proceed from there to a map of surface height, we must infer the relative values of $n(x,y)$ across the image plane. We do this by assuming the measured surface to be smooth and continuous and applying a phase-unwrapping algorithm [11]. Starting with the wrapped phase map, one data point is selected as an unwrapping seed point. Working outward from this seed point, the unwrapping algorithm compares its phase to the measured phase of an adjacent point. If the magnitude of the phase difference is found to be greater than π, the appropriate integer multiple of 2π is either added to or subtracted from this adjacent measurement in order to bring the phase difference to within $\pm\pi$. This point is then used as a new seed and the procedure is repeated. In this way, the unwrapped area of the phase map is expanded until all of the measurement points have been unwrapped.

At this stage, all terms of equation (2) have been determined and the test surface height $h(x,y)$ can be found within an arbitrary constant from the equation

$$h(x,y) + C = \frac{[\psi(x,y) + \phi]\lambda}{4\pi} \qquad (3)$$

where the constant C arises from the phase term ϕ on the left-hand-side of equation (2). This constant specifies the axial position of the test part relative to the reference surface, and is generally not of interest. Clearly, use of an unwrapping algorithm is only valid when the test surface is known to be continuous and without surface-height steps greater than a quarter of the measurement wavelength. Although most MEMS are multilayered structures, often containing step heights of one micrometer or more, we have not found this limitation unduly restrictive. Our data-analysis software allows an arbitrarily shaped region of interest to be defined within the captured image sequence. Provided that this region of interest does not contain large surface-height steps, use of the unwrapping algorithm is justified. By using additional measurement wavelengths, the requirement for surface continuity can, in principle, be relaxed [13, 14].

C. *Measurement of moving structures*

1) *Effect of detector integration-time on fringe contrast*

Sections A and B outlined the procedures by which phase-shifting techniques can be used to characterize static structures. When the test object is stationary, the interference pattern described by equation (1) does not change over time. If, however, the test structure moves, the phase term ψ becomes a function not only of spatial co-ordinates x and y, but also of time t. In terms of the time-dependent surface height $h(x,y,t)$ we can write the interference pattern as

$$I(x,y,t) = A(x,y) + B(x,y)\cos\left[\frac{4\pi h(x,y,t)}{\lambda} + \phi\right] \quad (4)$$

If we use an integrating detector to observe the interference pattern over a time interval Δt, the measured intensity $I_{meas}(x,y)$, can be expressed as the integral of $I(x,y,t)$ over Δt. If the integration time is sufficiently small that we can assume the speed of the test surface to be constant over Δt, this integral can be evaluated to give:

$$I_{meas}(x,y) = \int_{t_0-(\Delta t/2)}^{t_0+(\Delta t/2)} I(x,y,t)dt = \Delta t\left\{ A(x,y) + B(x,y)\cos\left[\frac{4\pi h(x,y,t_0)}{\lambda} + \phi\right]\frac{\sin\alpha}{\alpha}\right\} \quad (5)$$

w[illegible] s the time at the center of the integration period and $\alpha=2\pi v\Delta t/\lambda$. From equation (5), the apparent phase of the integrated fringe pattern is that corresponding to the position of the test surface at the center of the integration period. The effect of the $[\sin(\alpha)/\alpha]$ term is simply to reduce the fringe contrast as compared with the static case. Expressed in terms of the fringe visibility V (a standard measure of fringe contrast given by $V=[I_{max}-I_{min}]/[I_{max}+I_{min}]$) we have

$$V = V_0\frac{\sin\alpha}{\alpha} \quad (6)$$

where V_0 is the fringe visibility at zero velocity. The practical effect of reducing the fringe visibility is to lower the signal-to-noise ratio of the phase measurement. The mean value of the recovered phase is not sensitive to the fringe visibility provided that visibility remains constant over the time taken to acquire the five phase-shifted interferograms. Because the phase-shifting method recovers the phase independently for each image pixel, the technique is also insensitive to the variations in fringe visibility across the image plane that would result, for example, from different parts of a structure moving at different speeds. The position of the first zero of $[sin(\alpha)/\alpha]$, at $\alpha=\pi$, sets a practical upper limit on the maximum measurable velocity $v_{max}=\lambda/2\Delta t$ (the test-surface velocity at which the fringe contrast first drops to zero).

The integration time Δt may be governed either by the light sensor or, alternatively, by the light source. Standard CCD cameras do not generally permit integration times shorter than 10^{-4} seconds, corresponding to $v_{max}\approx 2.5$ mm/s at visible wavelengths. Velocities much higher than this are commonplace in MEMS. For example, a structure moving sinusoidally at 10 kHz with an amplitude of just 1 μm reaches a maximum speed of over 60 mm/s as it crosses the zero displacement position. We can avoid this limitation by using a laser diode driven by a pulse generator to shorten the effective integration time below 1 μs, while still allowing us to use a standard CCD camera to record the interferograms. In our present setup the pulse width is approximately 500 ns and the laser wavelength is 658 nm, which establishes $v_{max}\approx 660$ mm/s. This value is set by our drive circuit rather than by the laser diode itself (which has a modulation bandwidth in the GHz range).

2) Phase unwrapping for moving structures

As discussed in Section A above, because monochromatic interference patterns are periodic along the axial co-ordinate, measurements using single-wavelength interferometry have an inherent $2n\pi$ phase ambiguity. This ambiguity means that phase maps must be unwrapped by removing artificial 2π jumps before they can be properly interpreted in terms of surface height. A related issue arises in the interpretation of a sequence of time-resolved phase maps in terms of motion of the test part. Consider a measurement run in which the interferometer captures N sets of five phase-shifted interferograms, each set corresponding to a different time within the motion period. Substituting the measured intensities into equation (2), each set of interferograms is processed to generate a time-resolved, wrapped phase map.

To convert the resultant N phase maps to surface-height maps, each must be unwrapped individually starting from some seed point, as described above. Although the unwrapping process removes all artificial phase discontinuities within each individual phase map, it leaves open the possibility that such discontinuities will exist between adjacent unwrapped phase maps in the

measurement sequence. The uncertainty arises because motion of the unwrapping seed point (which should be chosen to be the same point within each phase map) can cause its true optical phase to cross one or more 2π boundaries over the measurement period, producing wrapping errors in its recovered position vector. The result, then, is a sequence of time-resolved surface-height maps that are offset by the wrapping errors of the original seed point over the motion period.

To remove these wrapping errors, we must also unwrap the measured *(phase, time)* vector along the time axis, at the seed point. This unwrapping gives us an N-element vector containing the phase corrections that must be applied to each of the N spatially unwrapped phase maps to give a true picture of the structure motion. As a consequence, the choice of the spatial unwrapping seed point is significant. Successful unwrapping along the time axis relies on the motion of the seed point between any two consecutive measurements being smaller than $\lambda/4$, so that the resulting phase difference is smaller than π. Therefore, for a suitable seed point to exist, N should be chosen such that the speed of the slowest moving point on the test structure does not exceed $\lambda Nf/4$, where f is the fundamental frequency of the motion being observed. If such a point does not exist on the test structure (i.e. if $N \leq 4v/\lambda f$ at some phase of the motion for all measured points), unwrapping along the time axis is not possible. In these cases, the relative motions of all points on the test structure are still recoverable, but not the absolute motion of the structure with respect to the fixed reference surface.

To aid in selection of an unwrapping seed point after data capture, our analysis software computes a figure of merit for each point in the image plane, designed to identify those points with small motion amplitude. The figure of merit is found by forming a weighted sum, over the N measurements, of the absolute wrapped phase differences between consecutive data points. For slow-moving points, these phase differences will tend to be close to 0 (where wrapping between data points has not occurred) or 2π (where it has). By giving more weight to phase differences around these values, the figure of merit indicates the likely suitability of each point to act as the unwrapping seed point. By displaying the calculated figures of merit as a false-color map, the analysis software then allows the user to choose an appropriate seed point.

IV. STATIC AND DYNAMIC CHARACTERIZATION OF A SCANNING MICROMIRROR

A. Mirror design

To demonstrate the capabilities of the interferometer system, we carried out a number of experiments on a surface-micromachined scanning micromirror. The mirror, a fold-up structure intended for video-display applications [15], was designed

at BSAC (UC Berkeley) and fabricated in the MCNC MUMPS foundry process. The general design and fabrication principles for this type of structure have already been described [16]. Figure 2 shows SEM images of the major elements of the device. The mirror itself (Figure 2(a)) is a 600 μm-wide polysilicon plate, fabricated in the 1.5 μm-thick MUMPS POLY2 layer, supported on two 2 μm-wide polysilicon torsion bars. The mirror rotates on the bars which are attached to a 4.25 μm-thick rectangular frame composed of a layer of silicon dioxide sandwiched between two polysilicon layers (MUMPS POLY1 and POLY2 layers). The mirror-and-frame structure is held on the substrate by two pin-and-staple hinges that allow it to be folded up at an angle of approximately 90 degrees to the chip. We manually fold-up the mirror using a probe tip to push on a slider that is attached to the back frame of the device (see Figure 2(a)).

The mirror is driven by an electrostatic combdrive fabricated parallel to the chip plane [17], as shown in Figure 2(a) and (c). The combdrive consists of two sets of interdigitated polysilicon fingers, one fixed and one movable, that experience an attractive force when a drive voltage is applied between them. A restoring force is provided by folded polysilicon springs that connect the movable comb shuttle to a number of substrate anchors. The combdrive is attached to the mirror by a compliant, torsional linkage (Figure 2(b)) that allows the mirror and frame to be folded out of the plane of the chip. As the combdrive moves, under the influence of the applied voltage, it pushes and pulls on the base of the mirror causing it to tilt about the axis defined by the supporting torsional springs. At resonance, such devices can achieve beam-scan angles as large as 15 degrees, at frequencies of several kHz [18].

An important performance metric for these micromirrors is the ratio of the total optical scan angle to the angular divergence of the beam reflected from the mirror at any instant. Assuming that scan jitter is negligible, this ratio determines how many separate, resolved spots of light the mirror can generate along the line traced by the scanned beam. An upper limit to the ratio, which we will call the *mirror resolution*, is set by diffraction at the mirror aperture [18]. For a mirror diameter D and light at wavelength λ, the diffraction-limited resolution is proportional to D/λ, the proportionality constant depending on the form of the illuminating beam and the criterion used to judge whether two adjacent spots are resolved. For a collimated illuminating beam, diffraction-limited resolution would be achieved for a precisely planar mirror surface. In practice, however, residual stresses and stress gradients in the polysilicon films, as well as forces introduced during fold-up, distort the mirror surface and increase the divergence of the reflected beam above the diffraction-limited value. In some cases, these distortions approximate simple optical aberrations (for example defocus) and can readily be corrected using off-chip lenses [15, 18].

Out-of-plane deformations that might be considered insignificant from the point-of-view of device mechanical behavior can, nevertheless, have a strong influence on optical performance. As a rule-of-thumb, the surface of a nominally plane mirror should depart from planarity by less than one tenth of a wavelength (approximately 50 nm for visible light) if its uncorrected performance is to be close to diffraction-limited. Such small deformations would clearly not be noticeable in SEM images, such as those in Figure 2, but are easily detectable using optical interferometry.

B. Static mirror characterization

The planarity of the micromirror described above was studied (in its nonactuated state) using the computer-controlled interferometer to produce a surface-height map, as described in Section III. The resultant map is shown in Figure 3, in which grayscale value is used to represent surface height. The contours superimposed on the map are spaced at 200 nm intervals of surface height, and the labels H and C mark the points of attachment of the torsional hinges and combdrive, respectively. The measurement shows the mirror to have a saddle-shaped deformation, with concave curvature along the axis joining the torsional hinges and convex curvature along the orthogonal axis. The measured peak-to-valley magnitude of the deformation is approximately 1.5 μm, a figure that is typical of micromirrors of this size that have been fabricated in the POLY2 layer of the MCNC MUMPS process [10, 18]. By fitting the measured surface to a second-order polynomial (a good approximation to a spheroid for small curvatures), the radii of curvature along the two orthogonal axes were found to be +54.5 mm (concave axis) and –67.8 mm (convex axis). Thus, to a good approximation, this mirror acts as an astigmatic focusing element, with two focal lengths equal to +27.3 mm (converging) and –33.9 mm (diverging). As will be discussed in section IV.C below, the surface-height map allows us to make an accurate calculation of the size and shape of the scanned beam, and thereby to evaluate the device optical performance. The map also permits us to specify external corrective optics to compensate for the static mirror curvature.

To quantify random noise in our data, we repeated the measurement of the static-mirror surface five times over a period of a few minutes, and compared the resulting surface-height maps. A subset of the results from these tests is given in the upper plot of Figure 4 which shows a section through the five sets of surface-height data along a line parallel to the torsion-hinge axis. A small offset has been added to each data set to allow the five measured profiles to be compared. Using the surface-height data from the whole mirror area (9958 measured points in each surface-height map), we calculated the root-mean-square (rms) difference between each pair of measurements. The largest of these rms differences (1.47 nm) was between the first and fourth data sets. The lower plot of Figure 4 shows the difference between these two data sets, sectioned along the same line used in the plot above it. The high measurement repeatability demonstrated here allows our system to detect motion at amplitudes down to the

nanometer scale. We believe that the main factors presently limiting repeatability are vibration, air currents, and small fluctuations in the laser power delivered to the interferometer.

C. Dynamic mirror characterization

One of the main strengths of our characterization system is its ability to measure large-amplitude motion (tens of μm out-of-plane) at many points on a structure in a short time. To demonstrate this, we studied the motion of the micromirror device described above under two different drive conditions. In both cases, the device was operated in air at room temperature and pressure. The experiments were designed to measure: (1) the frequencies and modeshapes of resonant modes excited by the electrostatic combdrive, and (2) the magnitude and shape of the mirror deformation produced by operating the device at its fundamental resonant frequency.

1) Investigation of resonant modes

As mentioned in section II, the square-wave-drive mode of the measurement system can be used to locate and characterize resonant modes over a broad frequency range. For any damped mechanical system, the motion that results after a holding force is removed is not periodic, but decays over time. Nevertheless, this motion can be characterized using the stroboscopic technique if it is repeatedly re-excited with a periodic drive force. To recover an accurate transfer function, the period of the drive force must be sufficiently long to allow the motion to damp down to close-to-zero amplitude before the structure is re-excited. We used a drive repetition rate of 60 Hz which allowed the mirror motion to drop to less than 1% of the starting amplitude before re-excitation. Because of the high brightness of the laser diode, the mean power in the pulsed beam was sufficient to allow recording of interferograms in the standard 30 ms camera exposure time using a 500 ns laser-pulse width. The illumination duty cycle was 3×10^{-5}. We took a sequence of 512 full-field measurements of the mirror and frame, spanning one half of the drive-signal period (the measurements occupied the time interval between the falling and rising edges of the square wave). These settings gave us a frequency resolution of 120 Hz and a cutoff frequency of 30.72 kHz. As stated in Section II, the cutoff frequency is determined by the effective rate at which the motion is sampled, and can be varied by altering the update rate of the waveform generator.

After aligning the micromirror in the interferometer, we were able to acquire the 512 sets of phase-shifted interferograms (a total of 2560 image frames) in less than ten minutes. These interferograms were then analyzed as described in Section II to produce a set of 512 time-resolved surface-height maps. For each point on the mirror surface, a *(position,time)* vector could then be extracted, showing the motion of that point over the 8.33 ms that separated the falling and rising edges of the drive signal.

Figure 5 shows the measured vector for just one such point near the mirror tip (the end furthest from the substrate). The observed motion closely resembles that of a simple-harmonic damped oscillator. Although the amplitude close to the end of the 8.33 ms period is only on the order of 30 nm, it is still clearly resolved by the interferometer.

By processing the measured *(position, time)* vector for each point on the mirror surface in the Fourier domain [19], a complete set of frequency-response functions (containing both amplitude and phase terms) was then generated. Figure 6 (a) shows a subset of these data: a plot of the measured amplitude against frequency and position for points lying on a line through the center of the mirror and perpendicular to the tilt axis (see Figure 6 (b)). The plot, which represents only a small fraction of the data gathered in this experiment (104 of the 9790 measured points on the mirror surface), uses a logarithmic scale for the amplitude and frequency axes and a linear scale for the position axis. Resonant modes show up as ridges running along lines of constant frequency, the variations in the height of each ridge revealing the spatial distribution of the corresponding mode amplitude along the selected line on the mirror. As can be seen in the figure, three distinct resonances were detected, at 4.43, 8.03 and 20.61 kHz. By considering the measured amplitude and phase data for all points on the mirror surface at these three frequencies, we were able to reconstruct estimates of the corresponding mode shapes (Figure 6 (c), (d) and (e)).

Referring again to Figure 6 (a), the large-amplitude ridge at 4.43 kHz results from a motion that is predominantly a mirror tilt about the torsion-hinge axis. This is the desired mirror motion for beam-scanning applications. The position of the tilt axis shows up in Figure 6 (a) as a pronounced trough; the motion amplitude being smallest at the pivot point. The motion at this frequency also includes a small mirror deformation as evidenced by the slight curvature of the contour lines of the corresponding mode-shape plot. The two higher-order modes have peak amplitudes that are approximately 30 times smaller than that of the fundamental mode. Consequently, their recovered mode shapes show some influence of measurement noise, but their essential features can still be discerned. The mode at 8.03 kHz appears to result from a left-right asymmetric bending of the mirror frame. In this mode, three of the four corners of the rectangular frame remain essentially fixed, while the fourth (one of the corners at the top of the frame) moves in- and out-of plane. The result is a small mirror deformation combined with an off-axis mirror tilt. This type of motion results from the play in the pin-and-staple and scissor hinges that allowed the mirror and frame to be folded out of the substrate plane [20]. The mode at 20.61 kHz was found to consist of mirror tilt about an axis parallel to the substrate plane combined with an alternating concave-convex bowl-shaped deformation. No significant frame motion was observed at this frequency.

In performing the measurements outlined above it was important to ensure that all significant resonant modes were sampled at a rate greater than or equal to the Nyquist rate (two samples per period). If this is not the case (that is, if the cutoff frequency is chosen too low), energy from resonances above the cutoff frequency will spill into the recovered spectrum and produce spurious peaks. To check that our chosen settings gave an accurate measure of the motion, we repeated the measurements described in this section using a higher cutoff frequency (46.08 kHz). Since there were no detectable shifts in the observed resonant peaks, we conclude that the 30.72 kHz cutoff frequency was high enough to sample all significant modes excited by the electrostatic combdrive.

2) Measurement of mirror characteristics using a sinusoidal drive signal

In the case of perfectly linear mechanical systems, modal analysis using a broadband excitation signal combined with Fourier-transform techniques (as described above) can provide a complete description of the system behavior. Many MEM systems, however, are significantly nonlinear [2]. Most nonlinear effects seen in MEM devices can be separated into two categories: (1) those that result from stiffening springs (i.e. springs departing from Hooke's Law), and (2) those caused by incomplete knowledge of the relationship between the applied signal and the resulting drive force. This second category is seen, for example, if the actuator is attached to the driven structure via a non-linear element, such as a scissor hinge. An experiment to observe damped mechanical oscillations, such as the one described above, reveals only nonlinearities in the first category because the actuator applies no force to the test structure during the measurement period (the time between the falling and rising edges of the square-wave drive signal). Some nonlinear effects may become apparent only when a structure is driven at large amplitude. For devices designed to be driven at resonance, a dc or low-frequency square-wave drive signal may not be able to generate sufficient displacement to give reliable information about device behavior under the intended operating conditions. In these cases, while a measurement of mechanical ringing may still be useful for providing a quick identification of resonant modes, it cannot necessarily be used to predict the detailed operating behavior of the device.

To test the operation of the micromirror under the conditions required by the video-display application, we therefore drove it with a 72 V (zero-peak), 2.2 kHz sine wave applied to the electrostatic combdrive. Assuming its motion is in-plane, the combdrive produces a force that is proportional to the square of the applied signal. Therefore a drive at 2.2 kHz was expected to excite, predominantly, the fundamental tilting mode that had been found at 4.43 kHz in the ringing measurements described above. By changing the drive frequency in steps and observing the changes in the fringe pattern as we varied the time delay of the laser- pulse train, we were able to confirm the primary resonant peak found using square-wave excitation. The verification was within the frequency increment allowed by our drive system (approximately 35 Hz in the 4 kHz frequency range). We then

made a sequence of 32 measurements with a 7.1 µs laser-pulse delay increment, spanning one complete period of the motion. The data acquisition time, after optical alignment of the micromirror, was less than ten minutes.

Analyzing the data as described in Section II, produced a sequence of time-resolved surface-height maps showing the mirror-surface variation and position throughout the scan period. The maximum amplitude of motion was 14.98 µm at the mirror tip (furthest from the substrate), corresponding to a mirror-scan angle of about 2° and a beam-scan angle of 4°. Figure 7 shows the measured *(position, time)* vector for one point near the mirror tip and compares it to a best-fit sine wave. The maximum deviation from the sine wave is 1.6% of the peak-to-peak amplitude. From the complete data set (32 surface-height maps) we could extract similar position vectors for each of the more than 75000 measurement points that are distributed over the surface of the mirror and support frame.

Figure 8 (a) shows five of the measured surface-height maps, corresponding to five different laser-pulse time-delays, spaced at 28.4 µs intervals and spanning one-half period of the mirror scan. In the uppermost plot, the mirror is tilted down from the plane of the support frame. Because of the mismatch between the vertical- and horizontal-axis scales, both the tilt angle and the deformation of the mirror are greatly exaggerated in these plots. Although the torsional springs attaching the mirror to the frame were close to our smallest resolvable feature size (2 µm wide) the system was still able to recover phase data along their whole length. This allowed phase unwrapping to proceed over the whole mirror and frame area. The frame itself has a static out-of-plane deformation of approximately 3 µm (peak-to-valley) over its 1000×800 µm^2 area. This deformation, which is well approximated by a spheroid with convex radii-of-curvature of 36 and 41 mm, is likely to be caused by stress gradients in the polysilicon and silicon dioxide films from which it is fabricated.

Referring again to Figure 8 (a) the progress of the scan can be traced by following the sequence of plots from the top to the bottom of the page. As the time delays of the laser pulse train were increased, the mirror was seen to tilt toward the plane of the support frame. At its extreme position (113.6 µs after the start of the scan) the mirror and frame were essentially coplanar. During the scan return (not shown in Figure 8), the mirror retraced these positions in symmetric fashion. Although not clearly visible in Figure 8 (a), the data reveal a small periodic deformation of the support frame with a maximum amplitude of 1.1 µm. Comparison of the shape of this deformation with the data gathered from square-wave excitation of the structure suggests some coupling of energy into the resonant mode observed at 8.03 kHz.

For the video-display application, characterizing the dynamic deformation of the mirror surface is critical because of the strong influence the surface quality has on the scanned spot size. In Figure 8 (a), some mirror deformation is visible, but it is small relative to the mirror tilt. By least-squares-fitting each time-resolved data set from the mirror surface (excluding the frame) to the equation of a plane, we can separate the tilt and deformation components of the motion. The sequence of plots in Figure 8 (b) shows the residual mirror-surface height, after subtracting the least-squares-fit plane from each of the data sets plotted in Figure 8 (a). Each of these plots, therefore, shows the measured three-dimensional shape of the micromirror at a particular point during the scan. As was the case for the static measurement (Figure 3), the mirror has a largely saddle-shaped out-of-plane deformation. However, in the dynamic case the peak-to-valley deformation changes by a factor of almost four as the mirror swings through a 2° angle. The mirror most closely approximates a plane when it is parallel to the support frame.

As mentioned in section IV.B, once the surface height of a mirror has been mapped, the size and shape of a beam reflected from it can be predicted. In the video-display application envisaged, one or more micromirrors scan a modulated beam to form a rastered image in the back focal plane of a lens [15, 18]. The intensity distribution of the scanned spot can be found from the measured optical phase over the mirror aperture via a Fourier-transform relationship [21]. To predict the time-dependent form of the scanned spot, we used the following procedure. First, each time-resolved phase map was used to derive a complex-valued aperture function with a modulus equal to 1 over the mirror surface and 0 elsewhere. The phase at each nonzero point of the aperture function was then set equal to the interferometrically measured phase for that point. Finally, a fast 2-D Fourier transform was performed for each aperture function and the squared modulus of the result was calculated. This gives a map of the output-beam intensity at the back focal plane of a lens assuming that the input beam to the mirror is perfectly collimated and has uniform intensity.

The left-hand column of Figure 8 (c) shows the results of these calculations for the five mirror measurements plotted in Figure 8 (b). The mapping between calculated intensity and gray levels has been optimized individually for each of the five images so that the details of the spot shape can be seen clearly in each case. To provide a scale by which to judge the mirror performance, we also calculated the intensity distribution that would result from a perfectly planar mirror of the same size and shape. This diffraction-limited spot size is shown, for comparison, at the bottom of the figure. As a check of our calculations, we used the collimated pulsed beam of the interferometer to make direct measurements of the scanned-spot distribution. This was accomplished by placing the CCD camera in the back focal plane of a lens and blocking off the reference mirror to eliminate the interference fringes. By varying the time delay of the laser-pulse train, we were then able to record the instantaneous intensity distribution of the reflected spot at any chosen time within the scan period. The results of this experiment are shown for

comparison in the right-hand column of Figure 8 (c). Again, the mapping between intensity and gray levels has been scaled for each individual image. Also, because of the limited dynamic range of the camera, some saturation effects are visible for the smaller spot sizes at the end of the sequence. The qualitative agreement between the directly and indirectly measured spot sizes is seen to be very good. It is important to note that the interferometric measurements from which the left-hand column of Figure 8 (c) is derived and the direct measurements shown in the right-hand column are not equivalent; many different surface-height maps can lead to the same intensity distribution. The spot-size measurements were used simply to check that our calculations from the measured surface heights were consistent with direct observations.

V. CONCLUSIONS

We have demonstrated a stroboscopic phase-shifting interferometer for dynamic characterization of MEMS structures. We have shown that the system can characterize motions at frequencies ranging from the tens of Hz to the tens of kHz and have observed out-of-plane measurement repeatabilities better than 1.5 nm. Two key features of the system enable rapid analysis of MEMS dynamics: (1) the ability to gather data over a two-dimensional sample area without the need for scanning, and (2) a computer controller that automates data capture. Phase-measuring algorithms combined with spatial and temporal phase-unwrapping methods allow us to analyze not only rigid-body motion, but also time-dependent deformations of micromechanical structures. The high modulation bandwidth of the laser diode used in the system permits measurement of surfaces moving with large amplitude (tens of μm) at kHz frequencies. Its high brightness allows measurements to be made at extremely low illumination duty cycles. We have demonstrated interferometric stroboscopic imaging at duty cycles as small as 3×10^{-5}, using the standard 30 ms exposure time of a CCD camera. Although the technique we present is particularly well suited to the analysis of micro-optical devices, it may also be applied to the study of actuated microstructures in general. We anticipate that this and other dynamic characterization tools will be key elements in the drive to bring complex MEMS from laboratory prototypes to practical commercial devices.

REFERENCES

[1] L. E. Drain, *The laser Doppler technique*. Chichester: John Wiley & Sons, 1980.

[2] K. L. Turner, S. A. Miller, P. G. Hartwell, N. C. MacDonald, S. H. Strogatz, and S. G. Adams, "Five parametric resonances in a microelectromechanical system," *Nature*, vol. 396, pp. 149-152, 1998.

[3] C. Q. Davis and D. M. Freeman, "Using a light microscope to measure motions with nanometer accuracy," *Optical Engineering*, vol. 37, pp. 1299-1304, 1998.

[4] D. M. Freeman, A. J. Aranyosi, M. J. Gordon, and S. S. Hong, "Multidimensional motion analysis of MEMS using computer microvision," presented at Solid-State Sensor and Actuator Workshop, Hilton Head Island, SC, 1998.

[5] C. Q. Davis and D. M. Freeman, "Statistics of subpixel registration algorithms based on spatiotemporal gradients or block matching," *Optical Engineering*, vol. 37, pp. 1290-1298, 1998.

[6] W. Hemmert, M. S. Mermelstein, and D. M. Freeman, "Nanometer resolution of three-dimensional motions using video interference microscopy," presented at MEMS 99, Orlando, FL, 1999.

[7] J. S. Harris, R. L. Fusek, and J. S. Marcheski, "Stroboscopic interferometer," *Applied Optics*, vol. 18, pp. 2368-2371, 1979.

[8] D. Malacara, M. Servin, and Z. Malacara, *Interferogram analysis for optical testing*, vol. 61. New York: Marcel Dekker, 1998.

[9] R. C. Gutierrez, K. V. Shcheglov, and T. K. Tang, "Pulsed-source interferometry for characterization of resonant micromachined structures," presented at Solid-State Sensor and Actuator Workshop, Hilton Head Island, SC, USA, 1998.

[10] M. R. Hart, R. A. Conant, K. Y. Lau, and R. S. Muller, "Time-resolved measurement of optical MEMS using stroboscopic interferometry," presented at Transducers '99, Sendai, Japan, 1999.

[11] J. E. Greivenkamp and J. H. Bruning, "Phase shifting interferometry," in *Optical Shop Testing*, D. Malacara, Ed., Second ed. New York: John Wiley & Sons, Inc, 1992, pp. 501-597.

[12] P. Hariharan, B. F. Oreb, and T. Eiju, "Digital phase-shifting interferometry: a simple error-compensating phase calculation algorithm," *Applied Optics*, vol. 26, pp. 2504-2506, 1987.

[13] Y.-Y. Cheng and J. C. Wyant, "Two-wavelength phase shifting interferometry," *Applied Optics*, vol. 23, pp. 4539-4543, 1984.

[14] Y.-Y. Cheng and J. C. Wyant, "Multiple-wavelength phase shifting interferometry," *Applied Optics*, vol. 24, pp. 804-807, 1985.

[15] R. A. Conant, P. M. Hagelin, U. Krishnamoorthy, O. Solgaard, K. Y. Lau, and R. S. Muller, "A raster-scanning full-motion video display using polysilicon micromachined mirrors," presented at Transducers '99, Sendai, Japan, 1999.

[16] M.-H. Kiang, O. Solgaard, K. Y. Lau, and R. S. Muller, "Electrostatic combdrive-actuated micromirrors for laser-beam scanning and positioning," *Journal of Microelectromechanical Systems*, vol. 7, pp. 27-37, 1998.

[17] W. C. Tang, T.-C. H. Nguyen, M. W. Judy, and R. T. Howe, "Electrostatic-comb drive of lateral polysilicon resonators," *Sensors and Actuators A (Physical)*, vol. A21, pp. 328-331, 1990.

[18] P. M. Hagelin and O. Solgaard, "Optical raster-scanning displays based on surface-micromachined polysilicon mirrors," *IEEE Journal of Selected Topics in Quantum Electronics*, vol. 5, pp. 67-74, 1999.

[19] D. J. Ewins, *Modal testing: theory and practice*. New York: Wiley, 1984.

[20] K. S. J. Pister, M. W. Judy, S. R. Burgett, and R. S. Fearing, "Microfabricated hinges," *Sensors and Actuators A (Physical)*, vol. A33, pp. 249-256, 1992.

[21] J. W. Goodman, *Introduction to Fourier Optics*, Second ed: McGraw-Hill, 1996.

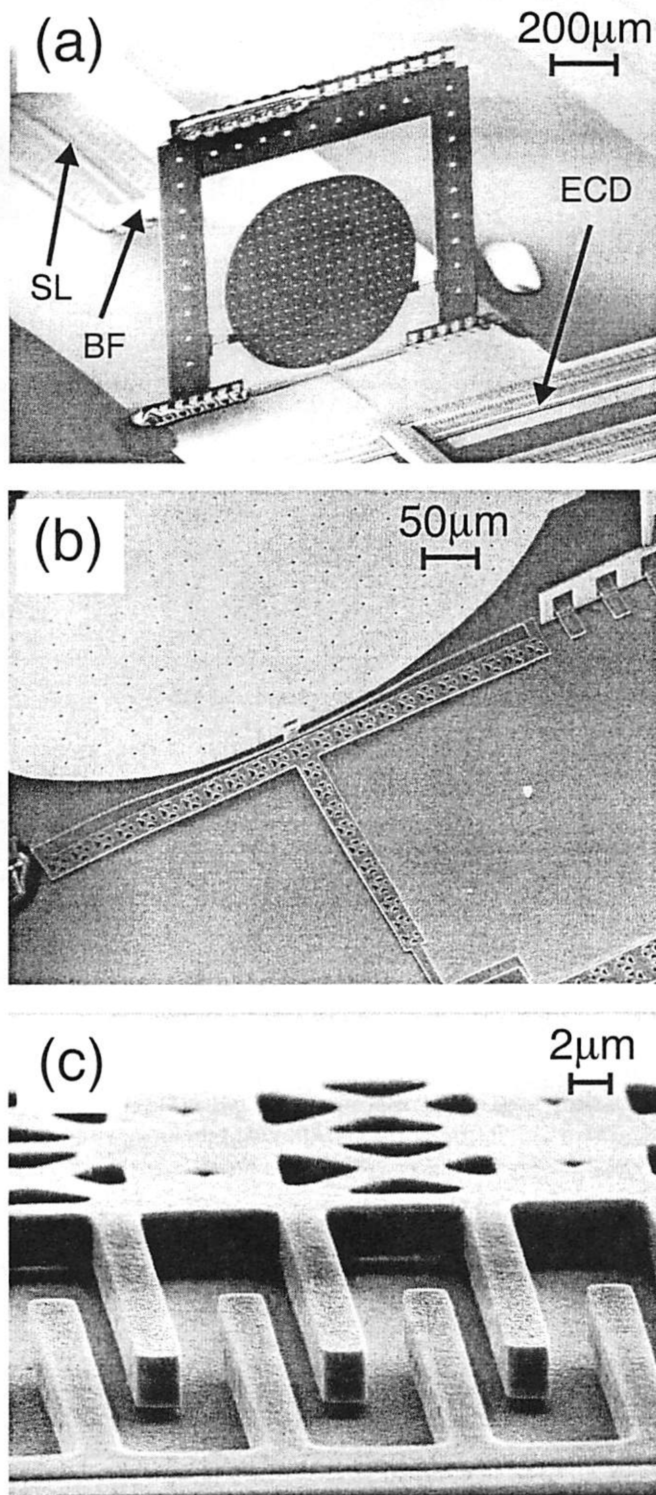

Figure 2: SEM images of (a) the fold-up mirror structure. Abbreviations used: SL – slider, BF – back frame, ESD – electrostatic combdrive. (b) The compliant linkage connecting the mirror to the drive, and (c) an enlarged view of part of the combdrive.

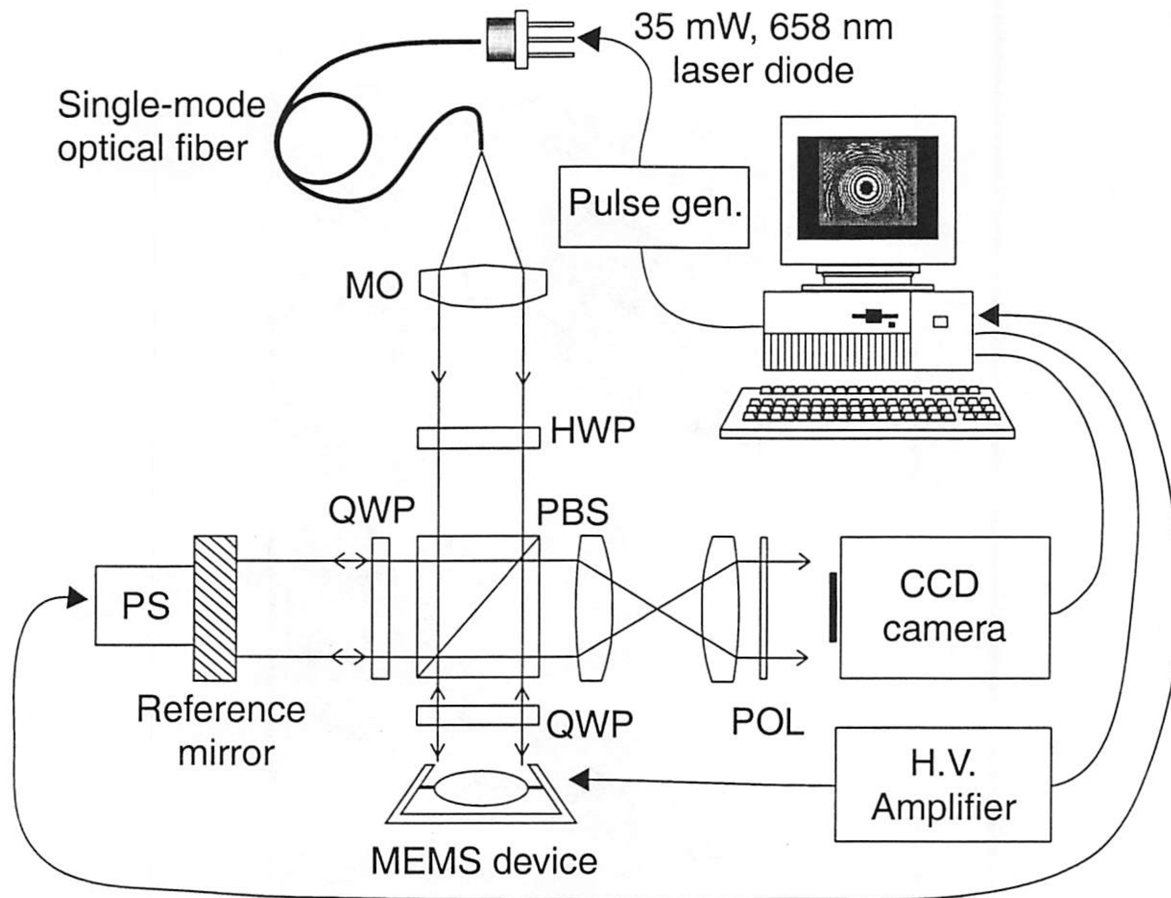

Figure 1: Experimental arrangement for the computer-controlled stroboscopic interferometer. The abbreviations used are as follows: MO – microscope objective, HWP – half-wave plate, QWP – quarter-wave plate, PS – piezoelectric stage, PBS – polarizing beamsplitter cube, POL – linear polarizer.

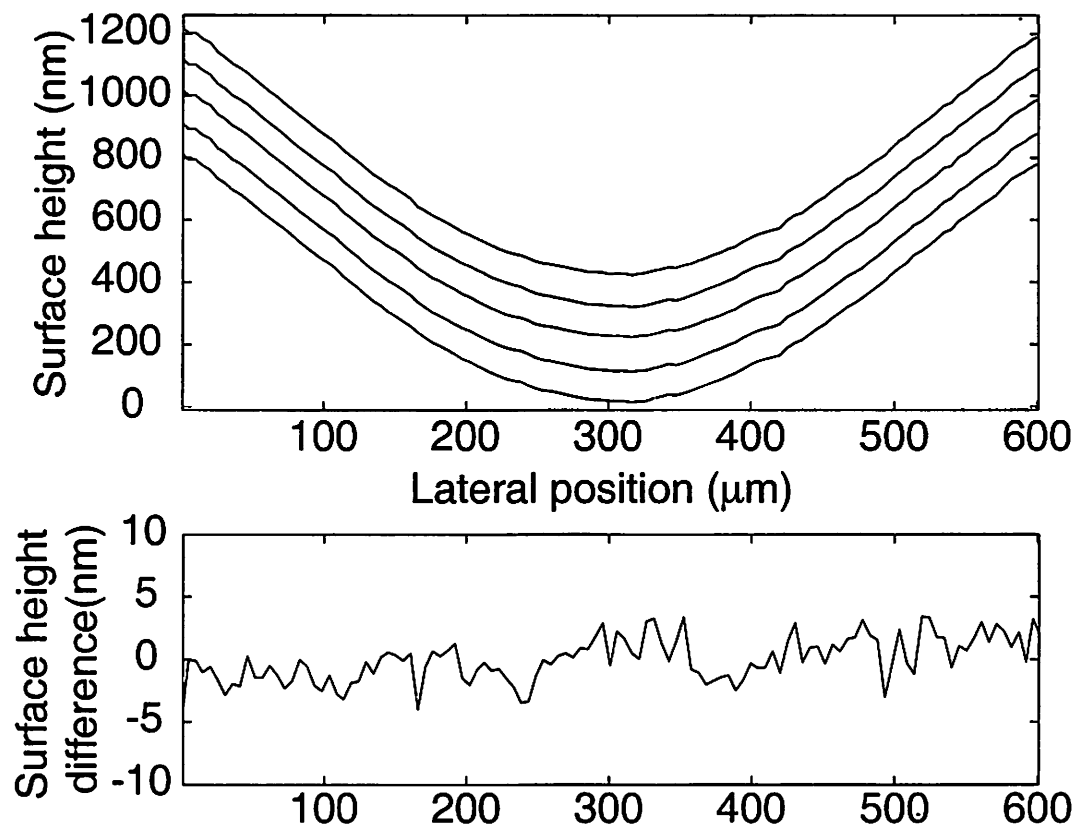

Figure 4: ***Top*** **- section through surface-height data from five successive measurements of static micromirror. The section was taken along a line parallel to the torsional-hinge axis. A small offset has been added to each data set, so that the five curves are all visible.** ***Bottom*** **- the surface height difference, along the same line, for the pair of measurements in worst agreement. For this pair of measurements, the r.m.s. surface-height difference over the whole mirror surface was found to be less than 1.5 nm.**

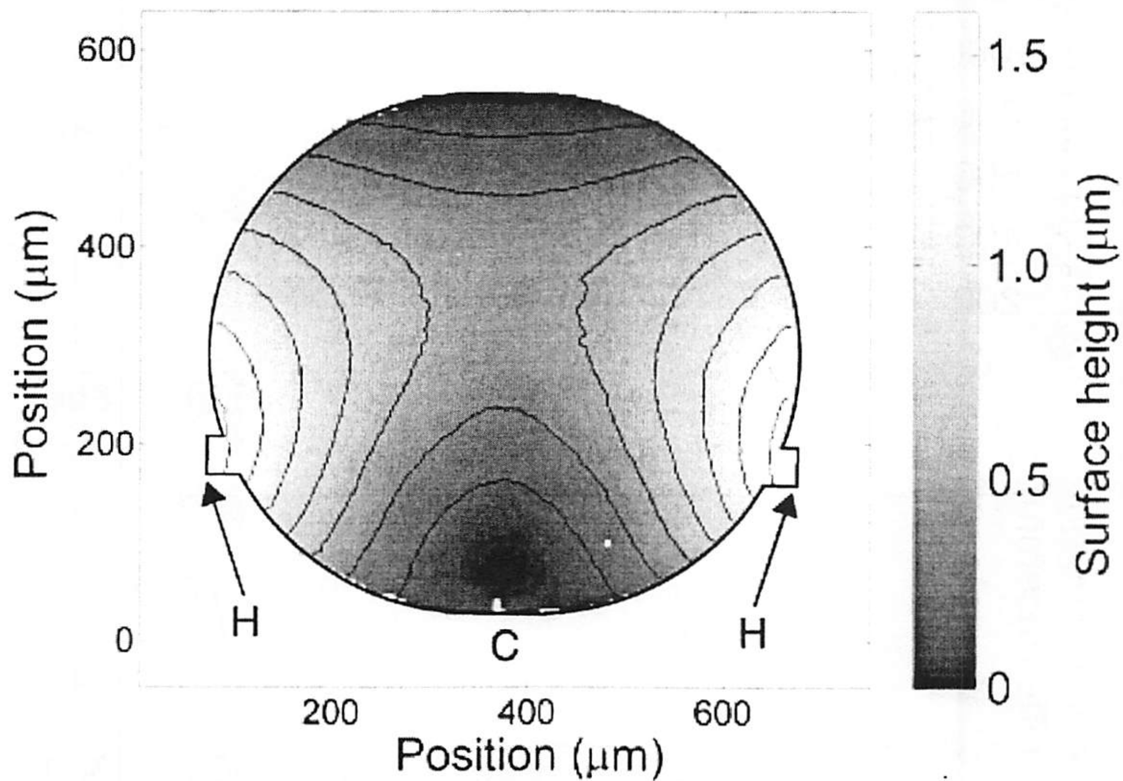

Figure 3: Measured surface-height map of static micromirror. The contour lines superimposed on the plot are spaced at 200 nm intervals. Points labeled H indicate where the torsional hinges attach to the mirror frame. The label C marks the point of attachment of the combdrive. The maximum departure from planarity is approximately 1.5 µm over the 600 µm-diameter of the mirror.

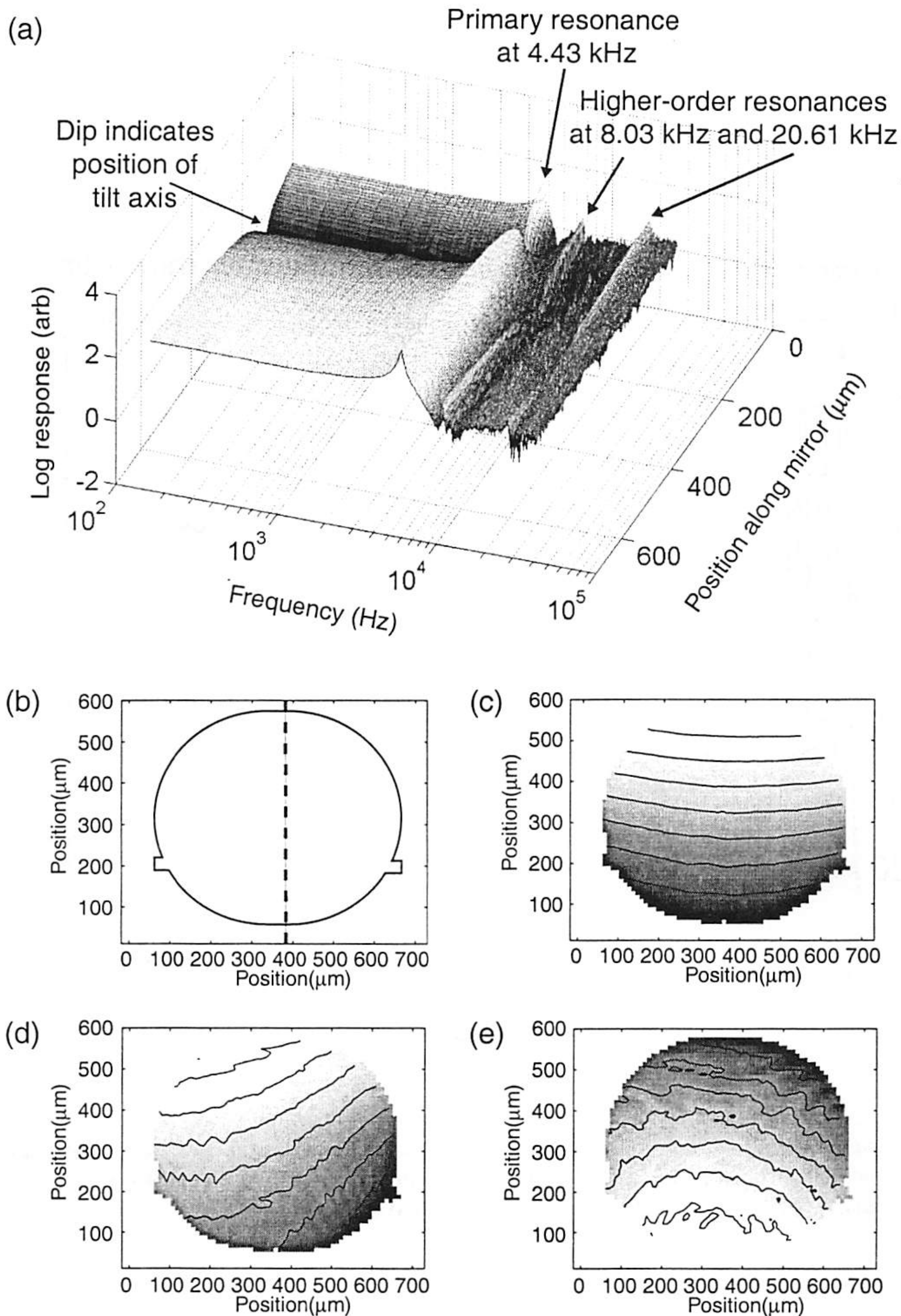

Figure 6: (a) Experimental logarithmic response for 104 separate points on the mirror surface, distributed along a line perpendicular to the tilt axis. The log(amplitude) data are plotted as a function of frequency (shown on a log scale) and lateral position. (b) Line on the mirror surface for which response data are plotted in (a). (c), (d) and (e) Modeshape estimates for resonant peaks observed at 4.43, 8.06 and 20.61 kHz respectively. Each of these three plots is a surface-height contour-map corresponding to one extreme of the motion seen at the specified frequency. The surface height scales are arbitrary. Lighter shading corresponds to larger surface-height values. The modeshape estimates were found by Fourier filtering of the measured (position, time) vectors at each point on the mirror surface. The lack of left-right symmetry in the mode seen at 8.06 kHz is the result of play in the scissor- and pin-and-staple hinges that allow the mirror and frame to be folded out of the substrate plane.

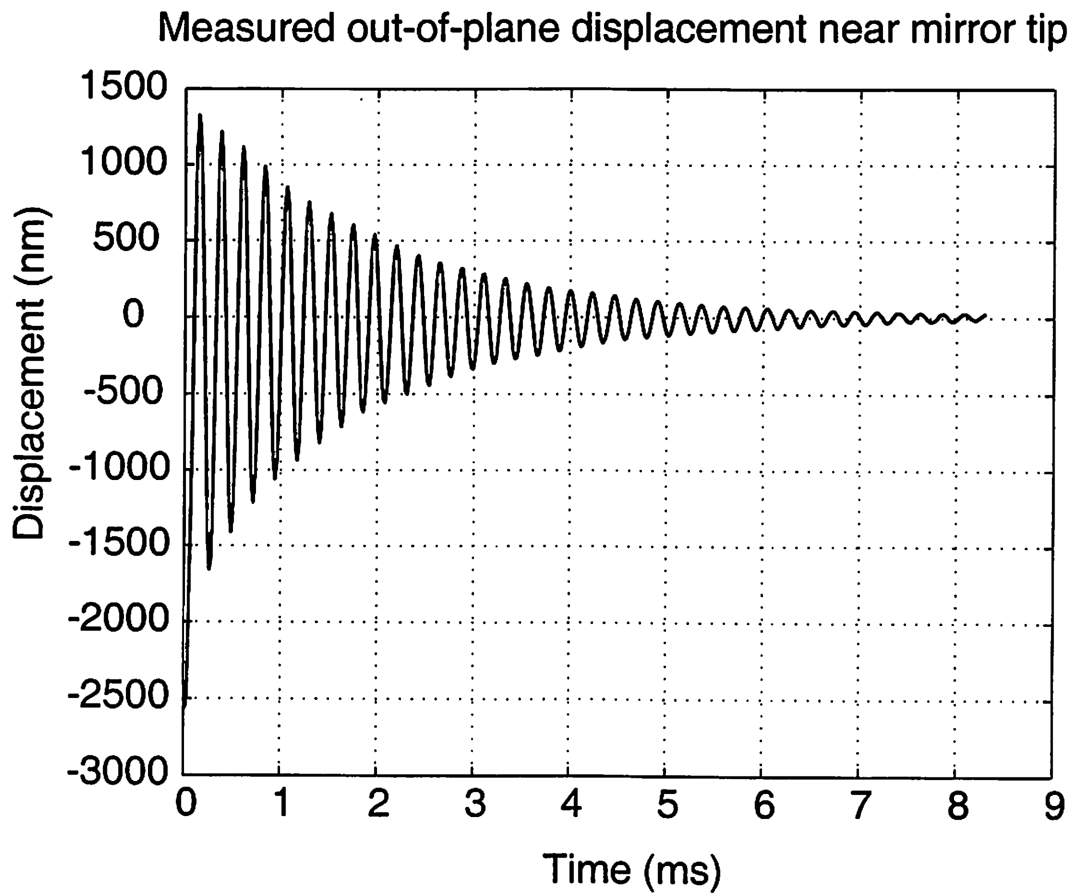

Figure 5: Measured position of one point on a micromirror over half the square-wave drive-signal period. Since the interferometer uses a stroboscopic technique, the measured data shown were acquired over many periods (approximately 3×10^4) of the drive signal.

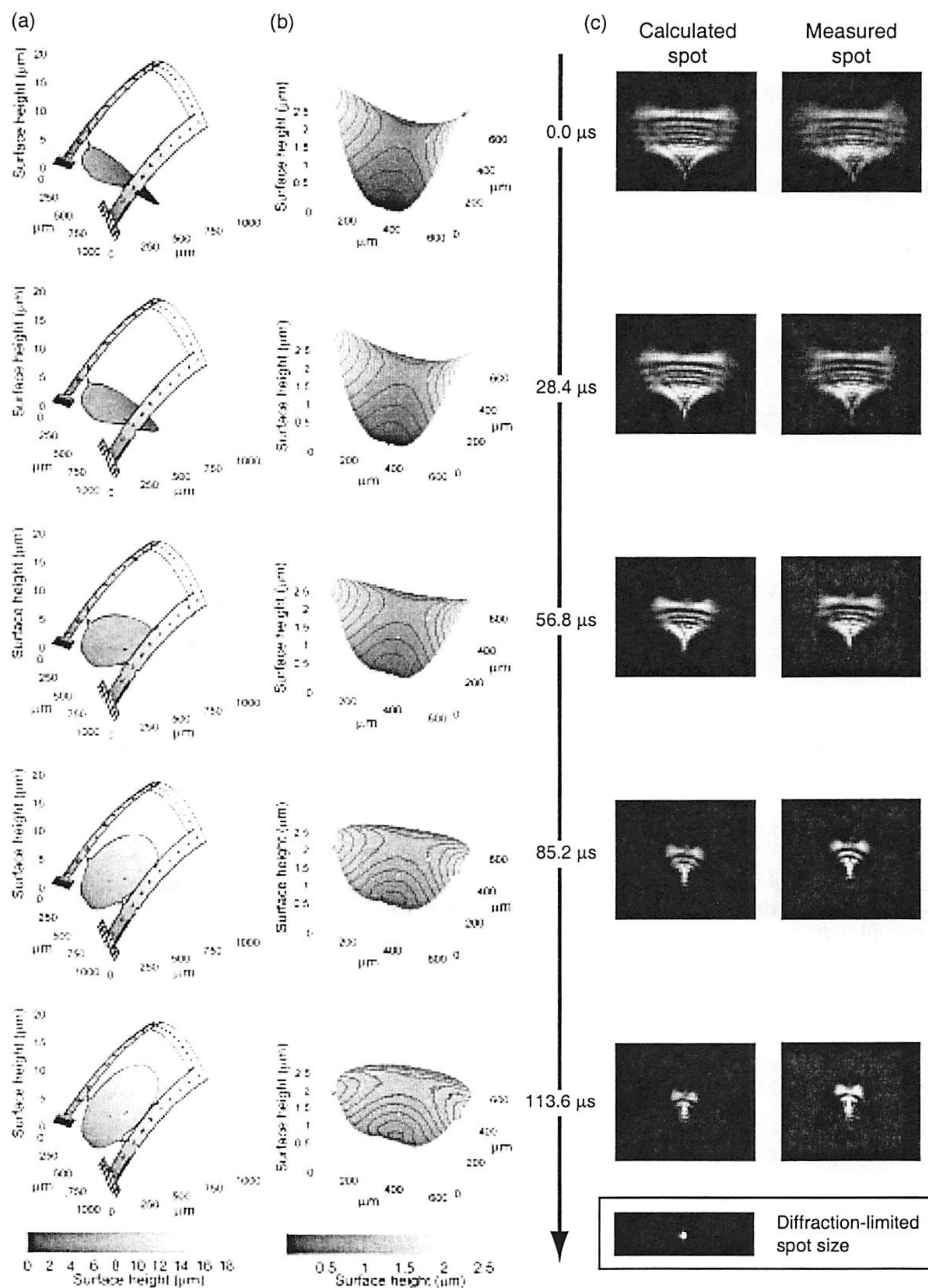

Figure 8: (a) Sequence of time-resolved surface-height measurements of polysilicon micromirror and frame. The mirror was scanning at its resonant frequency, 4.4 kHz. The measurements shown span one half period of the scanning motion and are spaced at 28.4 ms intervals. The large mismatch between the vertical and horizontal axis scales exaggerates the mirror scan angle, which was approximately 2 degrees. (b) Surface-height plots for the mirror alone, after subtraction of the gross tilt from each measurement. A saddle-shaped mirror deformation with a peak-to-valley surface-height difference of almost 3 microns can be seen in the uppermost plot. This deformation decreases steadily as the mirror tilts into the plane of the frame.
(c) Comparison of calculated and measured far-field spot sizes for each of the five micromirror positions.

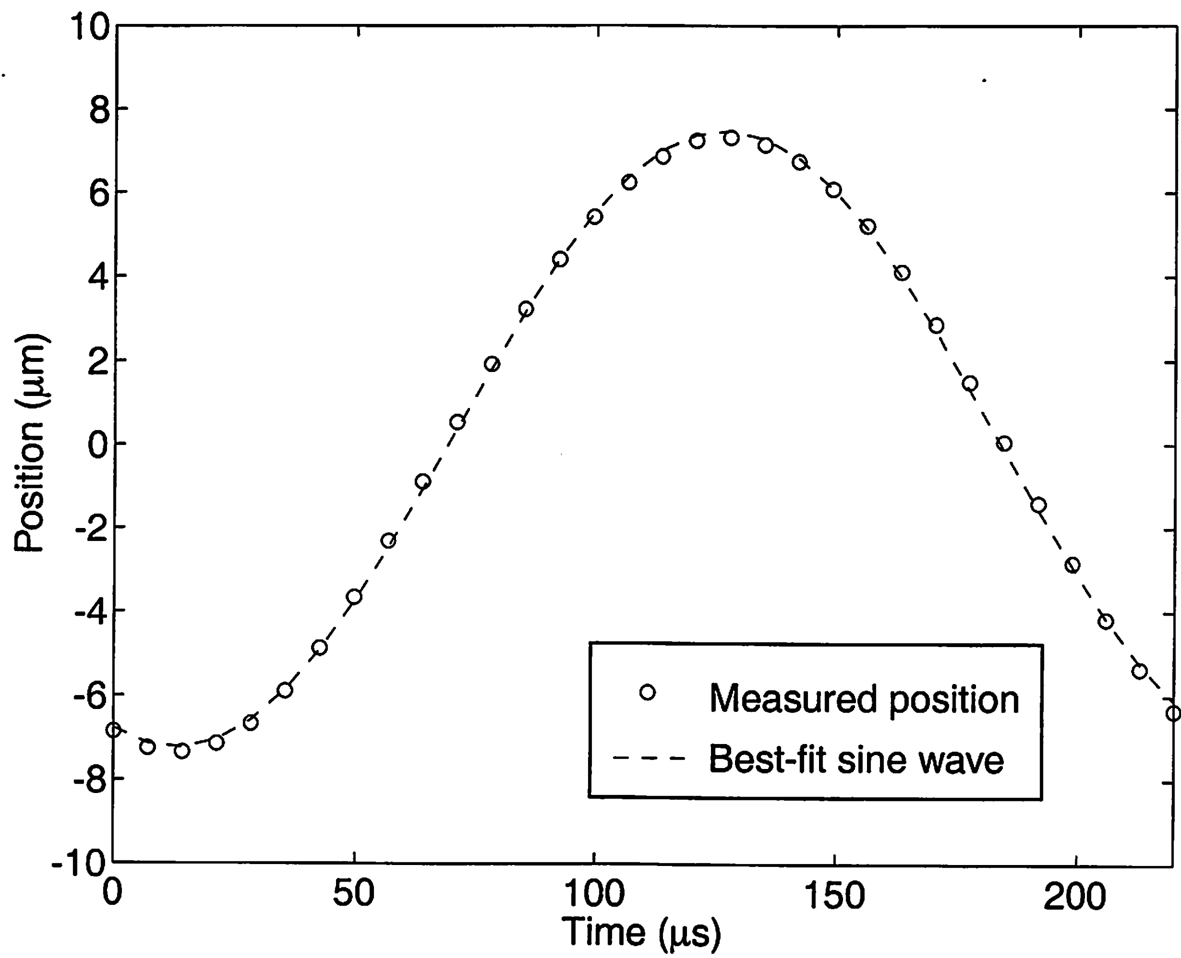

Figure 7: Measured *(position, time)* vector for a point near the mirror tip, shown together with best-fit sine wave. The maximum departure of the measured data from the sine wave is 0.16% of the motion amplitude.